ACS APPLIED ENERGY MATERIALS

Open Access

This article is licensed under CC-BY 4.0

www.acsaem.org

Article

Nature of Charge Carrier Recombination in $CuWO_4$ Photoanodes for Photoelectrochemical Water Splitting

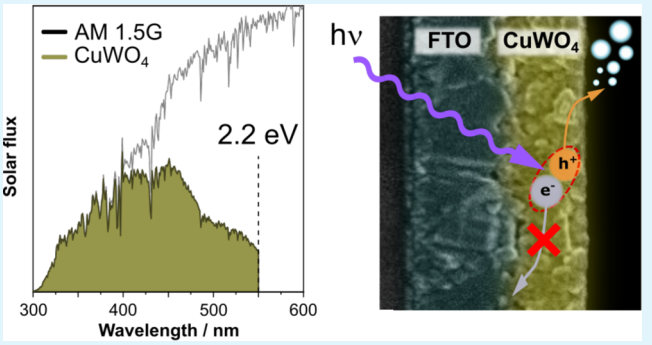
Ivan Grigioni,* Annalisa Polo, Chiara Nomellini, Laura Vigni, Alessandro Poma, Maria Vittoria Dozzi, and Elena Selli

Cite This: *ACS Appl. Energy Mater.* 2023, 6, 10020−10029

Read Online

ACCESS | Metrics & More | Article Recommendations | Supporting Information

ABSTRACT: $CuWO_4$ is a ternary semiconductor oxide with excellent visible light harvesting properties up to 550 nm and stability at high pH values, which make it a suitable material to build photoanodes for solar light conversion to hydrogen via water splitting. In this work, we studied the photoelectrochemical (PEC) performance of transparent $CuWO_4$ electrodes with tunable light absorption and thickness, aiming at identifying the intrinsic bottlenecks of photogenerated charge carriers in this semiconductor. We found that electrodes with optimal $CuWO_4$ thickness exhibit visible light activity due to the absorption of long-wavelength photons and a balanced electron and hole extraction from the oxide. The PEC performance of $CuWO_4$ is light-intensity-dependent, with charge recombination increasing with light intensity and most photogenerated charge carriers recombining in bulk sites, as demonstrated by PEC tests performed in the presence of sacrificial agents or cocatalysts. The best-performing 580 nm thick $CuWO_4$ electrode delivers a photocurrent of 0.37 mA cm^{-2} at 1.23 V_{SHE}, with a 7% absorbed photon to current efficiency over the $CuWO_4$ absorption spectrum.



KEYWORDS: *photoelectrocatalysis, ternary oxides, solar water splitting, solar light, renewable energy*

1. INTRODUCTION

Photoelectrochemical (PEC) water splitting produces clean O_2 and H_2 from water by exploiting sunlight directly.[1] The oxygen evolution reaction requires anodic semiconductor materials that are resistant to harsh reaction conditions. Moreover, an ideal material needs a narrow band gap to absorb a considerable portion of visible light and guarantee a solar to hydrogen efficiency above 10%, which is the lower limit for industrialization.[2,3]

Binary metal oxide-based photoelectrodes, such as WO_3 and α-Fe_2O_3,[4,5] initially attracted interest as visible-light-active materials. WO_3 has a high electron diffusion length and mobility,[4,6−8] and optimized electrodes allow almost complete absorbed photons to current conversion efficiency. However, WO_3 has poor chemical stability in neutral or basic pH and a relatively wide band gap (2.6−2.7 eV). On the other hand, hematite (Fe_2O_3) has an intriguing narrow band gap of 2.0 eV with potential solar to hydrogen conversion efficiency (η_{SHE}) up to 15% (Table 1),[9] but limited charge carrier lifetime (below 1 ns in undoped Fe_2O_3)[10,11] and mobility, which translate into suboptimal PEC performances.

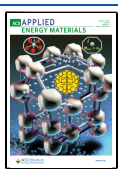
More recently, ternary oxides such as $BiVO_4$ with an intermediate band gap of 2.4 eV emerged as highly efficient materials for photoelectrocatalytic applications.[12−16] State-of-the-art $BiVO_4$ photoanodes show close-to-unity incident photon to current efficiency up to 480 nm.[17] However, the band gap of $BiVO_4$ is slightly larger than that desired for optimal photoanode materials. Indeed, a charge carrier recombination-free $BiVO_4$

Table 1. Commonly Used Semiconductor Oxide Photoanodes

semiconductor	BG[a]/eV	J_{max}[b]/mA cm^{-2}	η_{SHE}[c]
WO_3	2.6	4	5%
$BiVO_4$	2.4	7	8%
$CuWO_4$	2.2	10	12.5%
Fe_2O_3	2.0	12.5	15%
$CuMoWO_4$	2.0	12.5	15%

[a]bang gap (BG). [b]maximum current density (J_{max}). [c]solar to hydrogen efficiency (η_{SHE}) of semiconductor photoanodes assembled in a two-electrode tandem PEC cell, assuming complete light absorption and conversion of photons with energy larger than the band gap and 100% faradaic efficiency to H_2 and O_2.

Received: June 28, 2023
Accepted: September 1, 2023
Published: September 20, 2023



Downloaded from pubs.acs.org/aaemcq/article-pdf/6/19/10020/2967344/ae3c01608.pdf by guest on 30 August 2026

ACS Publications

© 2023 The Authors. Published by American Chemical Society

electrode (i.e., with an incident photon to current efficiency close to 100% up to the absorption onset at 520 nm) would lead to only 7−8% solar energy to hydrogen conversion, which implies that $BiVO_4$ should be used in combination with narrower band gap materials in complex multilayer photoanodes.[18]

Ternary $CuWO_4$ oxide has a band gap of 2.2 eV, and it could achieve an η_{SHE} of 12.5%.[19] Furthermore, the $CuWO_4$ band gap can be narrowed by substituting tungsten with molybdenum in quaternary $CuW_xMo_yO_4$. For example, $CuW_{0.5}Mo_{0.5}O_4$ has a band gap of 2.0 eV, corresponding to an absorption edge of 650 nm.[20−22] This tungstate family is stable in neutral and slightly basic pH because of the overlap between Cu 3d orbitals with O 2p orbitals.[23,24] This hybridization is also responsible for the negative shift of the $CuWO_4$ valence band compared to that of binary WO_3.[25] Moreover, $CuWO_4$ is suitable to assemble heterojunction systems with $BiVO_4$,[26,27] likewise WO_3.[28−32]

In prior studies, we investigated the charge carrier dynamics in transparent $CuWO_4$ electrodes and found that charge carriers mostly recombine within a 10 ps time scale, with only ca. 10% of them surviving longer than 1 ns to potentially run water oxidation.[33] In this work, we sought to experimentally study the intrinsic limits that hamper $CuWO_4$ photoactivity by employing a suite of PEC experiments to understand the factors shaping its performance. We prepared a series of thin-film $CuWO_4$ electrodes through a citrate-based aqueous solution method and tuned the $CuWO_4$ thickness to increase visible light exploitation of the photoanodes. To seek information on the charge carrier recombination processes occurring in bulk and surface $CuWO_4$ and on their implication in the overall PEC performance, we tested the electrodes under front- and back-side irradiation in both simulated solar light and monochromatic irradiation experiments. We also varied the light intensity to study the effect of the charge carrier density on the PEC activity and found that the PEC performance of $CuWO_4$ is light-intensity-dependent, with charge recombination increasing with light intensity, and that most photoproduced charge carriers recombine in bulk sites.

2. EXPERIMENTAL SECTION

2.1. Materials. The following chemicals were employed in the present work: copper(II) nitrate trihydrate (99% purity, Sigma-Aldrich), ammonium metatungstate hydrate $(NH_4)_6H_2W_{12}O_{40}\cdot xH_2O$ (99% purity, Fluka), citric acid (99% purity, Sigma-Aldrich), deionized water, boric acid (99.5% purity, Sigma-Aldrich), and KOH (99.5% purity, Sigma-Aldrich). All chemicals were used as received, with no further purification.

2.2. Photoelectrodes Preparation. The $CuWO_4$ thin films were prepared following a previously reported procedure.[33] Specifically, a 0.5 M solution of $CuWO_4$ was prepared by dissolving 14 mmol of citric acid in 5.3 mL of ethanol and 2.4 mL of deionized H_2O, followed by the addition of 5 mmol of $Cu(NO_3)_2\cdot 3H_2O$ under vigorous stirring and a stoichiometric amount of ammonium metatungstate hydrate. Fluorine-doped tin oxide (FTO) glass (Pilkington Glass, TEC-7, thickness of 2 mm) was used as conductive glass to prepare the FTO/$CuWO_4$ electrodes. The FTO glass was cleaned under sonication for 30 min in a soap-water solution, rinsed thoroughly with water, sonicated for 30 min in ethanol, and then dried in air. After cleaning, the electrodes were prepared by spin coating 100 μL of the $CuWO_4$ solution on FTO, at 4000 rpm for 30 s. Then, the $CuWO_4$ film was preannealed at 250 °C for 10 min and then annealed at 550 °C for 1 h. Prior to any test, the photoanodes were treated for about 30 s in a 0.5 M HCl aqueous solution to eventually eliminate any trace of CuO, then washed with distilled water and dried in air. The deposition, annealing, and HCl cleaning steps were repeated up to six times to prepare multilayer electrodes with the desired thickness and light absorption properties.

The $NiFeO_x$ cocatalyst was deposited onto the photoelectrodes employing a hydrothermal method,[34] by soaking the $CuWO_4$ electrode into an aqueous solution containing $NiCl_2$ (0.2 mM) and $FeCl_3$ (29.8 mM) as Ni^{2+} and Fe^{3+} sources in a closed vessel for 45 min at 100 °C.

2.3. Optical, Morphological, Structural, and Photoelectrochemical Tests. The absorption spectra of the $CuWO_4$ thin films on the electrodes were recorded in transmission mode with a Jasco V-650 spectrophotometer. The crystalline phase of the photoactive materials was determined by XRD analysis of the deposited thin films, using a Philips PW 1830/40 X-ray powder diffractometer equipped with a Cu tube at 40 kV and 40 mA. Top-view and cross-sectional field emission scanning electron microscopy (FESEM) images were acquired employing a LEO 1430 scanning electron microscope operating at a 10 kV accelerating voltage and an 8 mm working distance.

PEC measurements were performed using a homemade cell and an Autolab PGSTAT 12 potentiostat controlled by the NOVA software. In a typical setup, the electrode was used as the working electrode, a Pt wire was used as the counter electrode, and Ag/AgCl (3.0 M in NaCl) was used as the reference electrode. The photoanodes were tested under both back-side irradiation (through the FTO/$CuWO_4$ interface) and front-side irradiation (through the $CuWO_4$/FTO interface). The light source was an Oriel, Model 81172 Solar Simulator equipped with an AM 1.5 G filter. In simulated solar light irradiation experiments, the light intensity was measured with a Thorlab PM200 power meter equipped with a Si power head (S130VC) and set at 100 mW cm^{-2} (1 sun). In PEC experiments under simulated solar light with different intensities, a neutral light attenuator filter was employed to obtain 25 and 50 mW cm^{-2} intensities (0.25 and 0.5 sun, respectively) and a quartz lens was used to increase the intensity to 150 and 200 mA cm^{-2} (1.5 and 2 suns, respectively).

PEC experiments were carried out in a 0.1 M potassium borate (KBi) buffer solution at pH 9 unless otherwise stated. The potential vs Ag/AgCl was converted into the standard hydrogen electrode (SHE) scale using the following equation

$$E_{SHE} = E_{Ag/AgCl} + 0.059\ pH + E^{\circ}_{Ag/AgCl}$$
$$, \text{ with } E^{\circ}_{Ag/AgCl\ (3.0\ M\ NaCl)}$$
$$= 0.210\ V \text{ at } 25^{\circ}C$$

The incident photon-to-current efficiency (IPCE) was measured using a 300 W Lot-Oriel Xe lamp equipped with a Lot-Oriel Omni-λ 150 monochromator and a Thorlabs SC10 automatic shutter. A 1.23 V bias vs SHE (V_{SHE}) was applied, and the current was measured with a 10 nm step within the 350 to 600 nm wavelength range. The incident light power was measured at each wavelength by using a calibrated Thorlabs S130VC photodiode connected to a Thorlabs PM200 power meter. The IPCE at each wavelength was calculated using the following equation

$$IPCE_{\lambda} = \frac{1240 \times J_{\lambda}}{P_{\lambda} \times \lambda} \times 100$$

where J_{λ} is the photocurrent density (mA cm^{-2}) and P_{λ} (mW cm^{-2}) is the power of the monochromatic light at wavelength λ (nm).

The internal quantum efficiency (IQE) at each wavelength was calculated by combining the IPCE curve with the absorption (A) spectrum of each photoanode

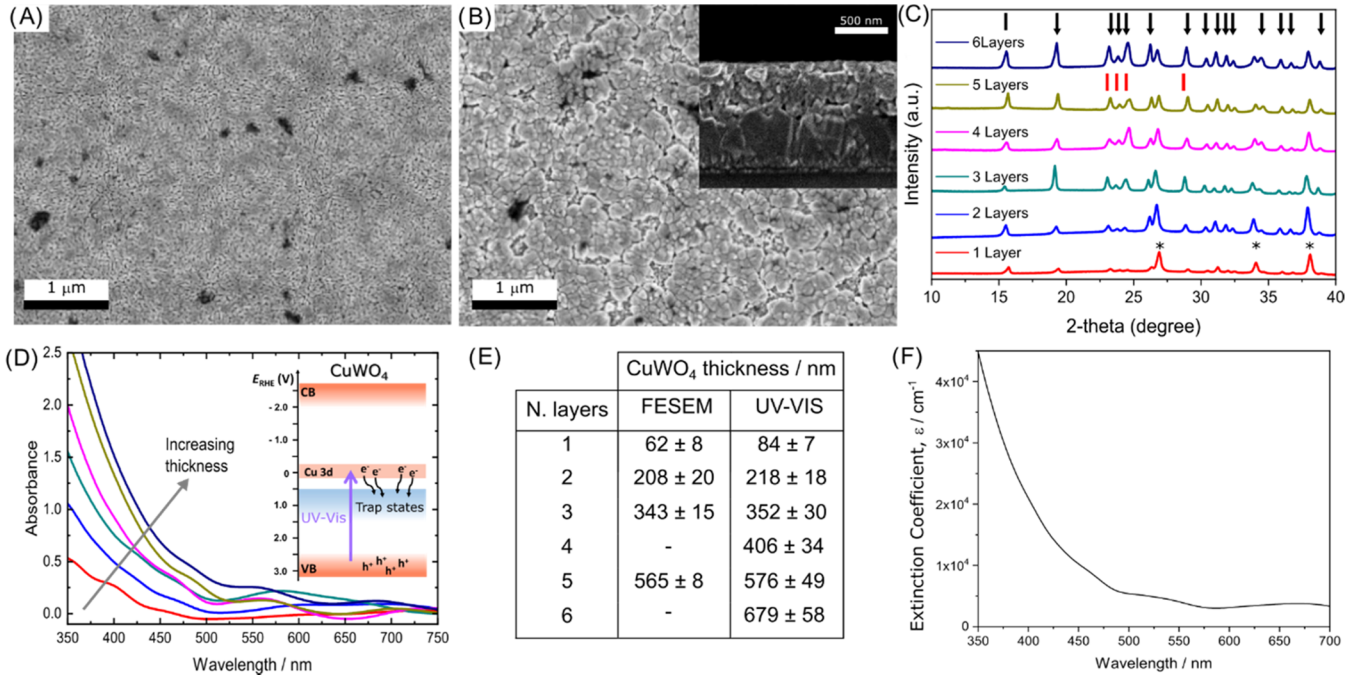
$$IQE_{\lambda} = \frac{IPCE_{\lambda}}{(1 - 10^{-A_{\lambda}})}$$

3. RESULTS

3.1. Characterization of $CuWO_4$ Multilayer Photoanodes. We started by studying the morphology of the $CuWO_4$ photoanodes by field emission scanning electron microscopy (FESEM). Top-view images (Figure 1A,B) reveal

Downloaded from pubs.acs.org/aaemcq/article-pdf/6/19/10020/2967344/ae3c01608.pdf by guest on 30 August 2026

https://doi.org/10.1021/acsaem.3c01608
ACS Appl. Energy Mater. 2023, 6, 10020−10029



N. layers	$CuWO_4$ thickness / nm	
	FESEM	UV-VIS
1	62 ± 8	84 ± 7
2	208 ± 20	218 ± 18
3	343 ± 15	352 ± 30
4	-	406 ± 34
5	565 ± 8	576 ± 49
6	-	679 ± 58

Figure 1. Field emission scanning electron microscopy (FESEM) top views of (A) 2 layers and (B) 5 layers of $CuWO_4$. Inset in (B): cross section of the $CuWO_4$ film obtained by depositing 5 layers. (C) XRD patterns of the $CuWO_4$ electrodes. The diffraction signals of WO_3 (JCPDF 89−4476), $CuWO_4$, and underlying FTO are identified with red bars, black arrows, and asterisks, respectively. (D) Absorption spectra of the $CuWO_4$ photoanodes with increasing semiconductor thickness. Inset: scheme of the optical transitions in $CuWO_4$. (E) Thickness of the electrodes with 1−6 $CuWO_4$ layers, from cross-sectional FESEM images (left column) and calculated from the absorption coefficient at 420 nm (right column). (F) Extinction coefficient vs wavelength of a 5-layered $CuWO_4$ electrode.

that $CuWO_4$ progressively covers the FTO substrate uniformly. Two deposited layers provide a continuous coating film consisting of oval-shaped nanostructures (Figure S1 in the Supporting Information). Bigger grains form in thicker electrodes (Figure 1B).

Cross-sectional images (inset of Figures 1B and S2) show that the $CuWO_4$ coating is compact along its whole thickness. Therefore, we could estimate the thickness of the photoactive layer in electrodes prepared with 1, 2, 3, and 5 $CuWO_4$ deposition cycles (Figure 1E).

The phase purity of the $CuWO_4$ films was assessed through XRD analysis and comparison with the Bragg reflections from JCPDF 72−0616, which revealed a triclinic structure (Figure 1C) and the absence of the WO_3 phase in all electrodes. Although no CuO phase is detectable in the XRD patterns, we washed the electrodes with diluted HCl to dissolve possible CuO impurity traces.

Then, we studied the optical properties of the electrodes by absorption spectroscopy in transmittance mode (Figure 1D). The multilayer films are optically transparent, with the absorbance in the UV region steeply increasing below 450 nm, without obvious absorption peaks consistently with the indirect forbidden d−d transition occurring in this Mott−Hubbard semiconductor,[35−37] possibly originating light scattering at wavelengths longer than 550 nm.

The main optical transition of $CuWO_4$ is assigned to the photoexcitation of electrons from the valence band, composed of O 2p states partly mixed with Cu 3d states, to the conduction band—empty Cu 3d levels (inset of Figure 1D).[33] A ca. 2.1 eV energy gap separates the band edges. $CuWO_4$ has an additional band of empty states at higher energy, i.e., at about 5 eV above the top of the valence band, consisting of W 5d and Cu 3d states. At wavelengths above 550 nm, scattering appears in the absorption spectrum of thicker films, possibly originating from the bigger grains observed in Figure 1B.

We combined the thickness values obtained from cross-sectional FESEM images and the absorption spectrum of $CuWO_4$ to estimate the absorption coefficient of $CuWO_4$ films at 420 nm (the edge between UV and visible light), using the following equation

$$A_{420} = \alpha_{420} \times d$$

where α_{420} (cm^{-1}) is the absorption coefficient of $CuWO_4$ at 420 nm, A_{420} is the absorption at 420 nm, and d is the average thickness in cm calculated from the cross-sectional FESEM images. From the A_{420} vs film thickness plot (see Figure S3), we calculated the absorption coefficient for $CuWO_4$ at 420 nm, $\alpha_{420} = (1.65 \pm 0.14)\ 10^4\ cm^{-1}$. This value is rather low compared to other semiconductor oxides, consistent with the indirect nature of the $CuWO_4$ band gap. For instance, it is 4-fold lower than the α_{420} value of $BiVO_4$ ($6.7 \times 10^4\ cm^{-1}$),[38] and this implies that to absorb the same amount of 420 nm photons, a $CuWO_4$ electrode needs to be 4 times thicker than a $BiVO_4$ electrode. Interestingly the absorption coefficient for $CuWO_4$ at 420 nm is also ca. 2-fold lower compared to $CuW_{0.5}Mo_{0.5}O_4$ ($3.41 \times 10^4\ cm^{-1}$),[20] which supports the hypothesis that Mo doping introduces additional optical transitions in $CuWO_4$.

The α_{420} for $CuWO_4$ value was then used to evaluate the thickness of the prepared $CuWO_4$ films from their absorbance at 420 nm. These thickness values are reported in Figure 1E. For convenience, hereafter, we identify the electrodes with different $CuWO_4$ thicknesses as $CuWO_4$:X, with X referring to the $CuWO_4$ thickness in nanometers (rounded to the nearest ten).

We also calculated the extinction coefficient of $CuWO_4$ at all wavelengths, based on the overall absorption spectrum of the thinnest electrode (which is moderately affected by scattering),

Downloaded from pubs.acs.org/aaemcq/article-pdf/6/19/10020/2967344/ae3c01608.pdf by guest on 30 August 2026

https://doi.org/10.1021/acsaem.3c01608
ACS Appl. Energy Mater. 2023, 6, 10020−10029

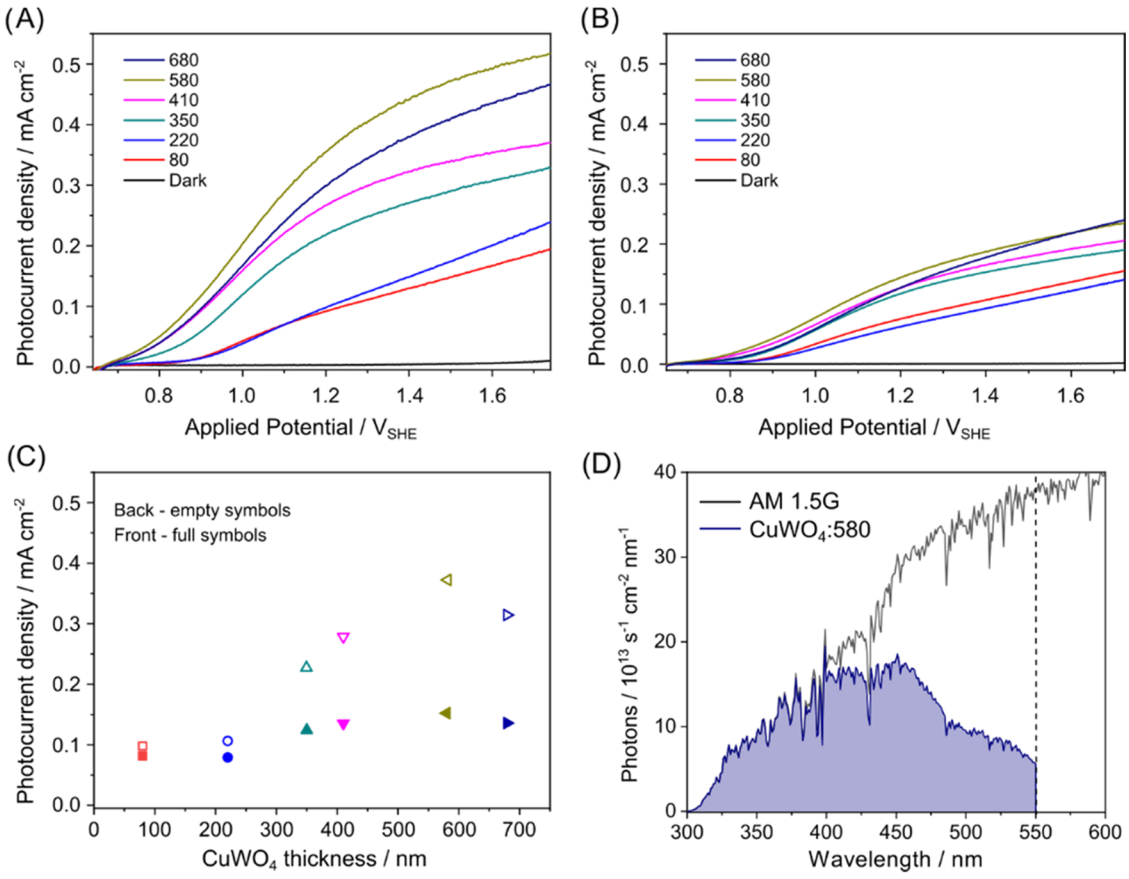


Figure 2. Linear sweep voltammetry (LSV) curves recorded with $CuWO_4$ multilayer photoanodes under (A) back-side or (B) front-side simulated solar light irradiation (100 mW cm^{-2}) in 0.1 M KBi buffer solution at pH 9. The labels within the figures refer to the thickness of the $CuWO_4$ layers, in nm. (C) Current density at 1.23 V_{SHE} as a function of the $CuWO_4$ thickness, under back- and front-side irradiation (empty and full symbols, respectively). (D) Overall photon flux in the AM 1.5 solar spectrum (black trace) and number of photons absorbed per second by $CuWO_4$:580 (blue area). The dashed vertical line marks the $CuWO_4$ absorption edge.

as $\alpha_\lambda = \frac{A_\lambda}{d}$, where A_λ is the absorbance over the 300−800 nm interval and d is the film thickness. The so estimated extinction coefficient of $CuWO_4$ vs wavelength is shown in Figure 1F.

3.2. Photoresponse of $CuWO_4$ Multilayer Photoanodes. We performed PEC experiments under monochromatic and simulated solar light irradiation to probe the photoresponse of the $CuWO_4$ electrodes with increasing thickness of the semiconductor layer. The experiments under simulated solar light provide information on their performance under conditions close to field application, while PEC tests performed under monochromatic irradiation provide information on the irradiation wavelength-dependent behavior of photoactive materials. We also tested the electrodes under back-side and front-side irradiation, i.e., with the light reaching $CuWO_4$ through the FTO or the electrolyte, respectively. Indeed the comparison between the PEC performance in the two modes proved diagnostic for identifying electron or hole transport as a limiting process in the illuminated semiconductor.[39,40]

Linear sweep voltammetry (LSV) tests performed under simulated solar light irradiation in 0.1 M borate buffer solution (KBi buffer) evidence that the photocurrent vs voltage increases with the $CuWO_4$ layer thickness (Figure 2A,B), up to a 580 nm thick $CuWO_4$ photoactive layer. Under back-side irradiation, the electrodes generate a larger photocurrent than under front-side irradiation (Figure 2C). For instance, the photocurrent of the $CuWO_4$:580 electrode under back irradiation is ≥2x than in the front-side mode.

Indeed, under front-side irradiation, most electrons are photogenerated far from the electron extraction site (the contact with the FTO layer). The lower photocurrent, compared to back-side irradiation, could indicate that electrons in $CuWO_4$ can travel only short distances because they undergo recombination with photogenerated holes within the film thickness, before reaching the extraction site. With the thinnest $CuWO_4$:80 electrode, similar photocurrents are recorded under front- and back-side irradiation (Figure 2A,B), demonstrating that photopromoted electrons can diffuse efficiently at least within a ca. 80 nm distance.

The best-performing $CuWO_4$:580 electrode generates a photocurrent density of 0.37 mA cm^{-2} at 1.23 V_{SHE} under back-side irradiation. This value is in line with previous records for $CuWO_4$-based electrodes prepared with different synthetic strategies (Table 2).[41,42] However, it is far from the maximum photocurrent expected for the 2.2 eV band gap of $CuWO_4$. Indeed, assuming that all absorbed photons in the $CuWO_4$:580 electrode (Figure 2D) are completely converted into current would lead to a 5.6 mA cm^{-2} theoretical maximum photoresponse under 1 sun illumination. Thus, the photogenerated current is only 6.7% of this maximum value, which implies that more than 90% of the photogenerated charge carriers undergo recombination.

Downloaded from pubs.acs.org/aaemcq/article-pdf/6/19/10020/2967344/ae3c01608.pdf by guest on 30 August 2026

https://doi.org/10.1021/acsaem.3c01608
ACS Appl. Energy Mater. 2023, 6, 10020−10029

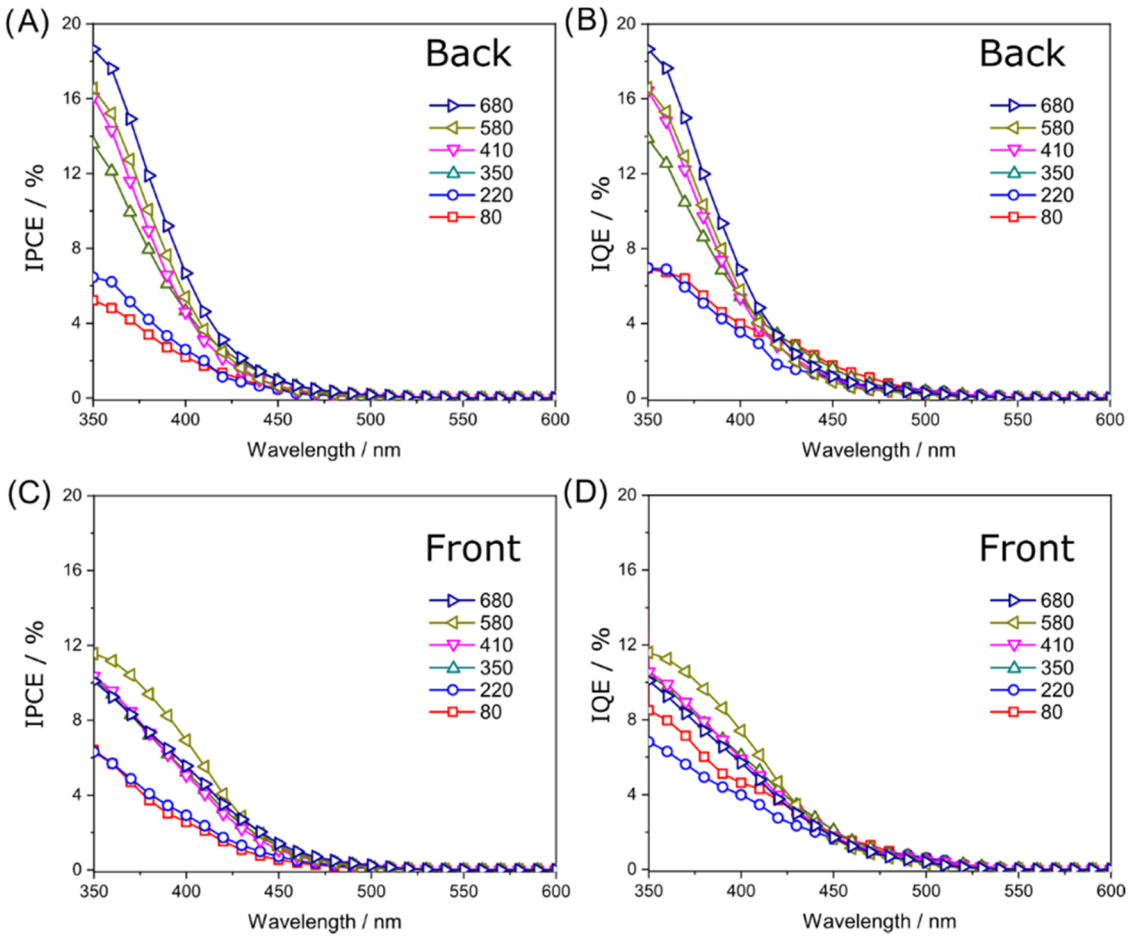


Figure 3. (A, C) IPCE and (B, D) IQE analyses of $CuWO_4$ multilayer photoanodes under (A, B) back-side and (C, D) front-side monochromatic irradiation, at 1.23 V_{SHE}.

Figure 3 shows the incident photon to current efficiency (IPCE) and internal quantum efficiency (IQE) curves recorded with the $CuWO_4$ photoanodes under back- and front-side irradiation at an applied bias of 1.23 V_{SHE}. All IPCE curves monotonously decrease with increasing incident wavelength without any defined peak or steep IPCE feature (Figure 3A,C). This suggests the presence of a single electronic transition with broad rather than sharp band edges within the investigated light energy. The IQE values (Figure 3B,D), which account for the number of absorbed photons which generate photocurrent and is equal to the charge transport efficiency,[53] are larger than the IPCE values. However, in this photoelectrode series, the IQE differs slightly from the corresponding IPCE values because of the relatively high electrode absorbance, especially in the UV region where the electrodes completely absorb the incident light. On the other hand, under visible light irradiation, when the electrodes absorb less than 50% of the incident light, the IQE is noticeably larger than the IPCE (Figure S4). The tests performed under monochromatic irradiation with the thickest electrodes pinpoint a $CuWO_4$ photocurrent onset at ca. 550−560 nm (we measured IPCE at high applied bias, 1.73 V_{SHE}, to increase the photocurrent signal close to the band gap excitation edge; see Figures S5 and S6), in good agreement with the reported 2.2−2.3 eV band gap of $CuWO_4$.

Under back-side irradiation, the $CuWO_4$ electrodes generate larger IPCEs than under front-side irradiation, implying that electron transport issues limit the overall photoresponse of this material and substantiating the behavior observed in LSV tests.[39]

Notably, under back-side irradiation, in LSV tests $CuWO_4$:580 outperforms the other electrodes (Figure 2A), while in IPCE, the thickest $CuWO_4$:680 electrode is best performing (Figure 3A). This difference relies on both the different light intensities (100 mW cm^{-2} in LSV analyses vs a few mW cm^{-2} in IPCE) and the poor electron transport of $CuWO_4$. Under back-side irradiation and the low light intensity employed in IPCE analyses, most photons are absorbed close to the FTO glass where electron extraction toward the external circuit easily occurs. However, a larger light intensity (e.g., under simulated solar light irradiation) generates a larger amount of excited electrons deep in the $CuWO_4$ film, far from FTO, at distances exceeding the mean electron diffusion within $CuWO_4$. These electrons are more likely to recombine with holes and limit the overall photocurrent in the thickest electrode.

3.3. Light Intensity Dependence. Employing the best-performing $CuWO_4$:580 photoelectrode, we evaluated the effect on photoactivity of the light intensity under back-side irradiation, to get further information on the charge separation efficiency within the $CuWO_4$ electrodes. For intensities larger than 1 sun, the measurements were carried out with the electrode in contact with a 0.5 M KBi electrolyte solution because the 0.1 M KBi electrolyte employed in LSV analyses under 1 sun irradiation (Figure 2) was insufficiently conductive

Downloaded from pubs.acs.org/aaemcq/article-pdf/6/19/10020/2967344/ae3c01608.pdf by guest on 30 August 2026

https://doi.org/10.1021/acsaem.3c01608
ACS Appl. Energy Mater. 2023, 6, 10020−10029

Table 2. Photoelectrochemical Performances of Literature Benchmark $CuWO_4$ Photoanodes Prepared with Different Synthetic Approaches

			J^g	stability		
synthetic method	electrolyte	thickness/nm	/ mA cm^{-2}	Time / min	$J_{fin}{}^h$ / mA cm^{-2}–^{2} $J_{fin}{}^h$	ref
spin-coating	0.1 M KPi (pH 7)	580	0.37	120	0.37	this work
one step-hy[a]	0.2 M KPi (pH 7)[e]	~1500	0.38	50	0.3	43
ST − hy[b]	0.1 M KPi (pH 7)	≥1000	~0.3	60	~5%[i]	44
ST − hy	0.1 M KPi (pH 7)	≥1000	0.34	240	~35%[i]	45
ST − hy	1 M KBi (pH 9)[f]	≥1000	0.4	60	0.39	29
ST − hy	0.1 M KPi (pH 7)	2000	0.42	n/a	n/a	46
ST − hy	0.1 M KPi (pH 7)	≥1000	0.35	240	0.26	47
spin-coating	KPi (pH 7)	500	0.47	600	0.4	48
e-deposition[c]	0.1 M KPi (pH 7)	2−3000	0.18	600	~50%[i]	25
ALD[d]	1 M KBi (pH 9.0)	80	~0.15	n/a	n/a	41
ST - hy	0.1 M Kpi (pH 7)	≥1000	0.35	60	~17%[i]	22
spin coating	0.1 M Na_2SO_4 (pH 6.8)	800	0.27	2.5	0.21	49
spray pyrolysis	0.1 M KPi (pH 7)	1.5−2000	0.19	n/a	n/a	50
spin coating	KPi/NaCl 0.1/0.14 M	250	0.38	n/a	n/a	51
ST − hy	0.1 M KPi (pH 7)	≥1000	0.38	240	0.39	52

[a]one-step hydrothermal. [b]sacrificial template−hydrothermal. [c]electrodeposition. [d]atomic layer deposition. [e]potassium phosphate buffer. [f]potassium borate buffer. [g]current density at 1.23 V_{SHE}, [h]current density at 1.23 V_{SHE} at the end of the stability test, [i]current density percent drop at the end of the stability test (in this case the stability is at a voltage ≥1.23 V_{SHE}).

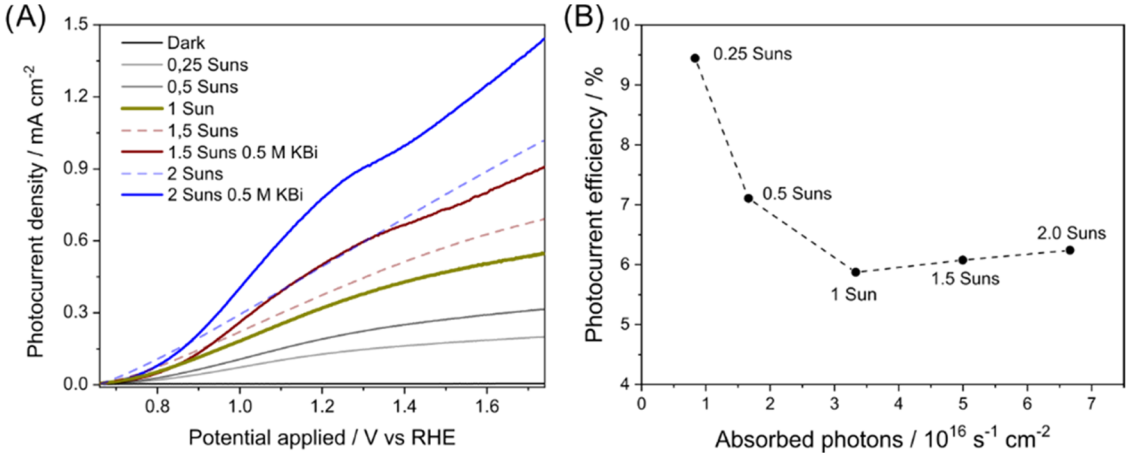


Figure 4. (A) LSV curves recorded with the $CuWO_4$:580 photoelectrode under different irradiation intensities in contact with 0.1 M (0−1 sun) or 0.5 M (1.5−2 sun) (continuous lines) KBi solutions. The two dashed lines are the LSV curves recorded under 1.5 and 2 sun irradiation in contact with 0.1 M KBi solutions. (B) Photocurrent efficiency at 1.23 V_{SHE} vs absorbed photons per unit time at different irradiation intensities.

to sustain photocurrents larger than 0.5 mA cm^{-2} (see dashed lines in Figure 4A).

The photocurrent response of the $CuWO_4$:580 photoelectrode increases with increasing light intensity (Figure 4A), though this increase is not linear. We thus calculated the absorbed photons to current efficiency (photocurrent efficiency) over the full solar spectrum at different light intensities by dividing the number of photopromoted electrons exiting the $CuWO_4$ film at 1.23 V_{SHE} by the total number of absorbed photons (Figure 2D, integrated blue area of the absorbed photons per nm). Figure 4B reports the photocurrent efficiency values vs the amount of absorbed photons per unit time.

The photocurrent efficiency decreases with increasing light intensity from 0.25 to 1 sun and stabilizes at ca. 6% for an illumination intensity greater than 1 sun (~3×10^{16} s^{-1} cm^{-2}). The drop from 0.25 to 1 sun is consistent with an increased charge carrier recombination at high photon flux, as found when comparing IPCE and LSV results, and could be related to inefficient bulk charge extraction at high light intensity.

3.4. Water Oxidation Kinetics of $CuWO_4$.

The PEC characterization of $CuWO_4$ photoanodes points to a photoactivity up to 550−560 nm and severe charge carrier recombination due to limited electron mobility in the bulk. To collect further information about this weak point of $CuWO_4$ photoefficiency, we sought to investigate the oxidation reaction and stability of this semiconductor. The results of such an analysis are reported in Figure 5.

We first compared the performance of $CuWO_4$ to that of an oxide affected by intrinsic sluggish surface water oxidation kinetics. We chose bismuth vanadate because we extensively studied it in previous studies and for its relatively poor photocatalytic activity in the oxygen evolution reaction.[54] As shown in Figure 5A, the photocurrent response of undoped $BiVO_4$ at 1.23 V_{SHE} rapidly decreases by more than 60% within a few seconds after the beginning of irradiation. This behavior is usually ascribed to surface hole accumulation due to the slow hole transfer across the semiconductor/electrolyte interface and consequent charge carrier recombination.

Downloaded from pubs.acs.org/aaemcq/article-pdf/6/19/10020/2967344/ae3c01608.pdf by guest on 30 August 2026

https://doi.org/10.1021/acsaem.3c01608
ACS Appl. Energy Mater. 2023, 6, 10020−10029

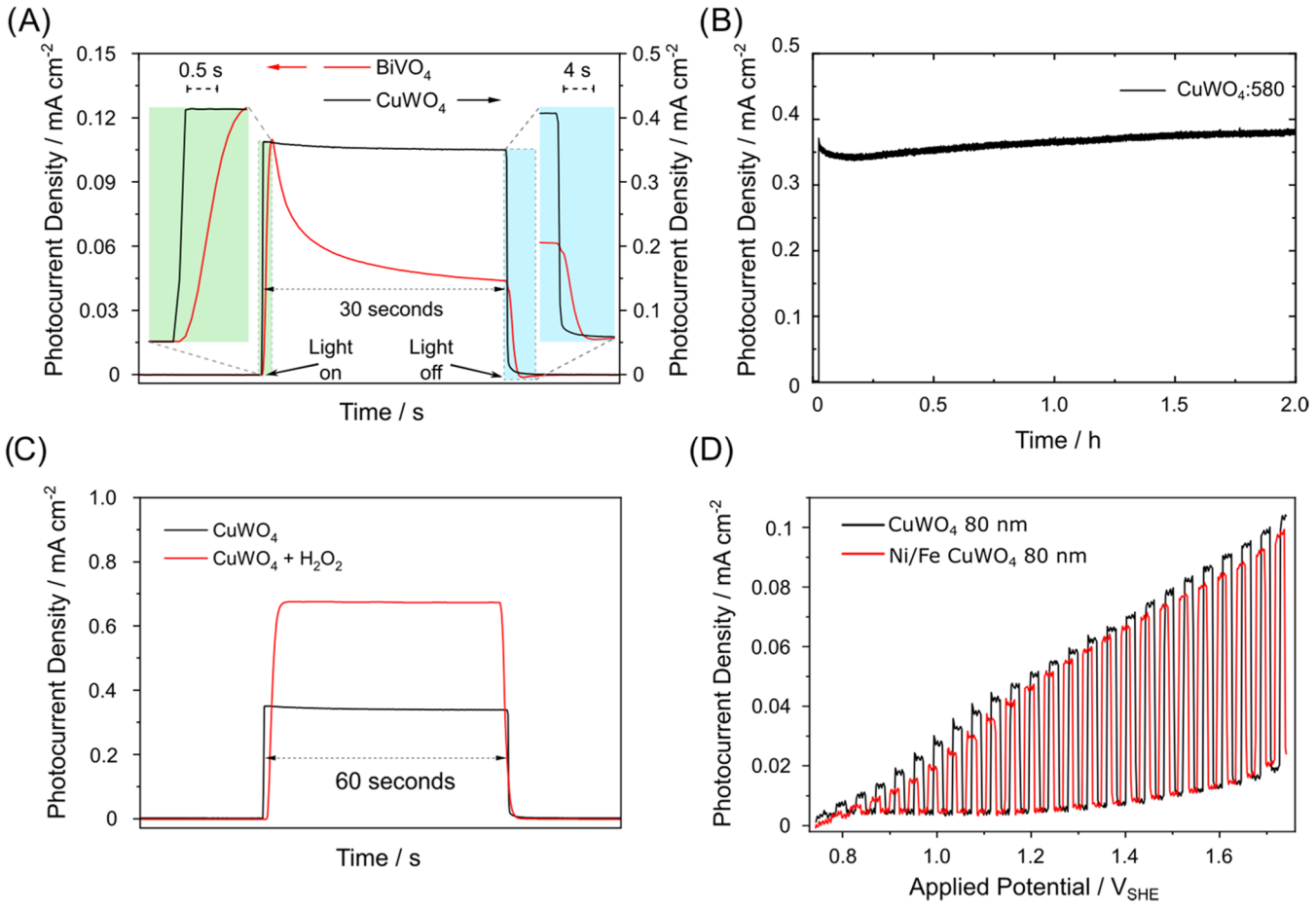


Figure 5. (A) Chopped chronoamperometry under 1 sun irradiation of an 80 nm thick $CuWO_4$ photoanode (black line) and a 75 nm thick $BiVO_4$ photoanode (red line), under back-side irradiation at 1.23 V_{SHE}. The green (light on) and blue (light off) boxes display expanded portions of the photocurrent curve. (B) Chronoamperometric stability test of the $CuWO_4$:580 electrode under simulated solar light irradiation in 0.1 M KBi. (C) Chopped chronoamperometry under 1 sun irradiation of the $CuWO_4$:580 photoanode in the presence (red line) or in the absence (black line) of 0.5 M H_2O_2. (D) Chopped LSV curves recorded with a bare (black line) and $NiFeO_x$-modified (red line) $CuWO_4$:80 photoanode under monochromatic irradiation at 420 nm; the light intensity is 9 mW cm^{-2}.

Moreover, when the light is switched off, a negative capacitive current appears for $BiVO_4$ due to the consumption of accumulated surface holes via recombination with electrons from the external circuit (a negative current indicates a reductive process taking place at the working electrode). On the other hand, the $CuWO_4$ photoanode shows a sharp photocurrent onset and negligible photocurrent decrease under irradiation, and a sharp decrease when the light is turned on and off, respectively (Figure 5A). These behaviors point to low hole accumulation at the $CuWO_4$ surface; that is, consumption of surface holes occurs right after they reach the electrode/electrolyte interface. We also checked the stability of the $CuWO_4$ electrode and found a negligible activity drop during a 2 h test (see Figure 5B), supporting the low hole accumulation at the surface and the chemical stability of this semiconductor.

To probe the nature of the electron−hole recombination, we performed PEC experiments in the presence of a more feasible oxidation reaction. To do so, we tested the $CuWO_4$:580 electrode with an electrolyte containing H_2O_2 as an electron donor. Hydrogen peroxide is much more easily oxidizable than water (+0.68 V_{SHE} vs 1.23 V_{SHE} for water) and has a higher reaction rate (H_2O_2 to H_2O is a 2-hole process, while H_2O to O_2 is a 4-hole process).[24] The current doubled to 0.67 mA cm^{-2} at 1.23 V_{SHE} in the presence of H_2O_2 (Figure 5C). However, this increase is quite limited compared to $BiVO_4$, for which photocurrent increases from a few μA to mA in contact with electron-donor-containing solutions.[55,56] The moderate photocurrent increase in $CuWO_4$ suggests that the few holes reaching the photocatalyst surface can very efficiently undergo oxidation reactions (i.e., water or electron donor oxidation). This experimental evidence rules out sluggish surface electron transfer as the main performance bottleneck in these photoactive films and indicates that the low PEC efficiency of $CuWO_4$ stems far from the surface catalytic sites.

To further check this hypothesis, we deposited a nickel−iron oxyhydroxide water oxidation catalyst on top of $CuWO_4$. $NiFeO_x$ ad-layers usually enhance the PEC performance of semiconductors which are limited by poor water oxidation kinetics (e.g., $BiVO_4$ or Ta_3O_5) or by low chemical stability (Si, or CdTe).[54,57,58] PEC analyses showed no performance enhancement for the $NiFeO_x$-modified $CuWO_4$ photoanode compared to the bare one (Figure 5D). The negligible effect of the $NiFeO_x$ cocatalyst confirms the intrinsic activity of surface $CuWO_4$ sites and that, therefore, photogenerated charge carriers recombine far from the semiconductor/electrolyte interface.

Downloaded from pubs.acs.org/aaemcq/article-pdf/6/19/10020/2967344/aae3c01608.pdf by guest on 30 August 2026

https://doi.org/10.1021/acsaem.3c01608
ACS Appl. Energy Mater. 2023, 6, 10020−10029

4. DISCUSSION

The spin coating preparation technique employed here offers a simple way to tune the $CuWO_4$ thickness and reach a desirable trade-off between visible light absorption and electron−hole separation, resulting in optimal PEC performances. The highest current density achieved (0.37 mA cm^{-2} with the 580 nm thick $CuWO_4$ electrode) aligns with the benchmark literature reports (Table 2). The thickness of the best-performing photoanode (580 nm) is similar to that of transparent electrodes prepared by Tian et al. with a spin-coating synthesis (500 nm),[48] suggesting that the optimal balance between absorption and charge separation in undoped, bulk, and polycrystalline $CuWO_4$ is within 5−600 nm. Recently, facet control along the 100 crystal facet showed improved conductivity and enhanced current density (0.38 mA cm^{-2}) in bulk 1.5 μm thick $CuWO_4$ films.[43]

Nanostructuring provides efficient charge carrier transport.[59] Indeed, $CuWO_4$ electrodes with nanoflake morphology[22,29,44−47,52] facilitate hole extraction from the oxide flakes because their 30−60 nm width is within the hole diffusion length in $CuWO_4$. However, the film thickness ($\geq$1 μm) exceeds electron diffusion in $CuWO_4$ and likely limits the PEC performance to ~0.4 mA cm^{-2}.

Doping and mild reduction via hydrogenation of semiconductors offer further control of the defectivity and charge carrier density. For example, Mo doping in $BiVO_4$ improves PEC performances by increasing electron mobility, disfavoring recombination, and enhancing charge separation.[60,61] These strategies induce similar chemical and electronic effects in $CuWO_4$ and translate into efficiency improvements (from 0.30 to 0.39 mA cm^{-2} for hydrogenation,[44] from 0.35 to 0.62 mA cm^{-2} for Mo doping,[22] from 0.27 to 0.42 mA cm^{-2} for Fe doping,[49,50] from 0.38 to 0.57 mA cm^{-2} for fluorine doping).[52]

The moderate photocurrent increase observed with $CuWO_4$ in the presence of hole scavengers such as H_2O_2 (Figure 5C) indicates that few holes reach the electrode/electrolyte interface, where they are rapidly consumed at surface catalytic sites.[41] This could be behind the slight photocurrent increase reported in previous work with Co-based oxygen evolution cocatalysts (from 0.34 to 0.42 mA cm^{-2} with CoPi,[45] from 0.32 to 0.54 with $CoIrO_x$,[47] and from 0.4 to 0.5 mA cm^{-2} with Co_3O_4).[48] In this work, we observed that the PEC performance of $CuWO_4$ photoanodes is unmodified after coating them with $NiFeO_x$. The lack of change in photoactivity could rely on the ineffective junction between the two materials. These findings further support the fact that Co-based oxygen evolution catalysts are more suitable to enhance the activity of $CuWO_4$ than Ni- and Fe-based ones. The simple synthesis reported here could offer a good platform to further enhance the $CuWO_4$ performance via these synthetic and postsynthetic approaches.

5. CONCLUSIONS

$CuWO_4$ photoanodes are good candidates for PEC water splitting applications. In fact, $CuWO_4$ is very photostable and, compared with other semiconductor oxides, has a high intrinsic activity of the surface catalytic sites for water oxidation. On the other hand, PEC tests under front- and back-side irradiation confirm the low mobility of photoelectrons in $CuWO_4$ and indicate that more than 90% of photogenerated charge carriers recombine in the bulk, which heavily limits the photon to current efficiency of $CuWO_4$. The higher quantum efficiencies at low light intensities (e.g., IPCE or below 1 sun) indicate that charge separation becomes less efficient at high photogenerated charge carrier densities and that charge recombination occurs mainly in bulk at defects or interface states. Therefore, $CuWO_4$ electrode optimization requires reducing this internal charge recombination through: (i) nanostructuring, to facilitate electron extraction toward FTO; (ii) defect engineering, to minimize the presence of recombination centers; and (iii) doping the crystalline structure, to act on the electronic states of the material and modulate its charge transport properties.

■ ASSOCIATED CONTENT

Supporting Information

The Supporting Information is available free of charge at https://pubs.acs.org/doi/10.1021/acsaem.3c01608.

Field emission electron microscopy images, absorbance vs thickness plot, IPCE and IQE plot for the $CuWO_4$-350 electrode, IPCE at 1.73 V_{SHE} (PDF)

■ AUTHOR INFORMATION

Corresponding Author

Ivan Grigioni − *Dipartimento di Chimica, Università degli Studi di Milano, 20133 Milano, Italy;* orcid.org/0000-0002-9469-4570; Email: ivan.grigioni@unimi.it

Authors

Annalisa Polo − *Dipartimento di Chimica, Università degli Studi di Milano, 20133 Milano, Italy;* orcid.org/0000-0001-5724-2607

Chiara Nomellini − *Dipartimento di Chimica, Università degli Studi di Milano, 20133 Milano, Italy*

Laura Vigni − *Dipartimento di Chimica, Università degli Studi di Milano, 20133 Milano, Italy*

Alessandro Poma − *Dipartimento di Chimica, Università degli Studi di Milano, 20133 Milano, Italy*

Maria Vittoria Dozzi − *Dipartimento di Chimica, Università degli Studi di Milano, 20133 Milano, Italy;* orcid.org/0000-0002-6390-9348

Elena Selli − *Dipartimento di Chimica, Università degli Studi di Milano, 20133 Milano, Italy;* orcid.org/0000-0001-8391-7639

Complete contact information is available at: https://pubs.acs.org/10.1021/acsaem.3c01608

Notes

The authors declare no competing financial interest.

■ ACKNOWLEDGMENTS

This work was supported by the Cariplo Foundation through the Project 2021-0664 entitled "Carbon dioxide conversion into energy-rich molecules with tailored catalysts" (CO2EnRich). I.G. acknowledges the European Union's Horizon 2020 research and innovation programme under Marie Sklodowska-Curie grant (agreement no. 846107).

■ REFERENCES

(1) Hisatomi, T.; Kubota, J.; Domen, K. Recent Advances in Semiconductors for Photocatalytic and Photoelectrochemical Water Splitting. *Chem. Soc. Rev.* **2014**, *43*, 7520−7535.

(2) Bard, A. J.; Fox, M. A. Artificial Photosynthesis: Solar Splitting of Water to Hydrogen and Oxygen. *Acc. Chem. Res.* **1995**, *28*, 141−145.

(3) Cowan, A. J.; Barnett, C. J.; Pendlebury, S. R.; Barroso, M.; Sivula, K.; Grätzel, M.; Durrant, J. R.; Klug, D. R. Activation Energies for the Rate-Limiting Step in Water Photooxidation by Nanostructured α-Fe_2O_3 Nd TiO_2. *J. Am. Chem. Soc.* **2011**, *133*, 10134−10140.

Downloaded from pubs.acs.org/aaemcq/article-pdf/6/19/10020/2967344/ae3c01608.pdf by guest on 30 August 2026

(4) Alexander, B. D.; Kulesza, P. J.; Rutkowska, I.; Solarska, R.; Augustynski, J. Metal Oxide Photoanodes for Solar Hydrogen Production. *J. Mater. Chem.* **2008**, *18*, 2298−2303.
(5) Tilley, S. D.; Cornuz, M.; Sivula, K.; Grätzel, M. Light-Inducedwater Splitting with Hematite: Improved Nanostructure and Iridium Oxide Catalysis. *Angew. Chem., Int. Ed.* **2010**, *49*, 6405−6408.
(6) Wang, H.; Lindgren, T.; He, J.; Hagfeldt, A.; Lindquist, S. E. Photolelectrochemistry of Nanostructured WO_3 Thin Film Electrodes for Water Oxidation: Mechanism of Electron Transport. *J. Phys. Chem. B* **2000**, *104*, 5686−5696.
(7) Reyes-Gil, K. R.; Wiggenhorn, C.; Brunschwig, B. S.; Lewis, N. S. Comparison between the Quantum Yields of Compact and Porous WO_3 Photoanodes. *J. Phys. Chem. C* **2013**, *117*, 14947−14957.
(8) Li, H.; Lin, C.; Yang, Y.; Dong, C.; Min, Y.; Shi, X.; Wang, L.; Lu, S.; Zhang, K. Boosting Reactive Oxygen Species Generation Using Inter-Facet Edge Rich WO_3 Arrays for Photoelectrochemical Conversion. *Angew. Chem., Int. Ed.* **2023**, *62*, No. e202210804, DOI: 10.1002/anie.202210804.
(9) Prévot, M. S.; Sivula, K. Photoelectrochemical Tandem Cells for Solar Water Splitting. *J. Phys. Chem. C* **2013**, *117*, 17879−17893.
(10) Huang, Z.; Lin, Y.; Xiang, X.; Rodríguez-Córdoba, W.; McDonald, K. J.; Hagen, K. S.; Choi, K.-S.; Brunschwig, B. S.; Musaev, D. G.; Hill, C. L.; Wang, D.; Lian, T. In Situ Probe of Photocarrier Dynamics in Water-Splitting Hematite (α-Fe2O3) Electrodes. *Energy Environ. Sci.* **2012**, *5*, 8923.
(11) Cherepy, N. J.; Liston, D. B.; Lovejoy, J. A.; Deng, H.; Zhang, J. Z. Ultrafast Studies of Photoexcited Electron Dynamics in γ- and r-Fe_2O_3 Semiconductor Nanoparticles. *J. Phys. Chem. B* **1998**, *5647*, 770−776, DOI: 10.1021/jp973149e.
(12) Kim, T. W.; Choi, K. S. Nanoporous $BiVO_4$ Photoanodes with Dual-Layer Oxygen Evolution Catalysts for Solar Water Splitting. *Science* **2014**, *343*, 990−994.
(13) Park, Y.; Mc Donald, K. J.; Choi, K. S. Progress in Bismuth Vanadate Photoanodes for Use in Solar Water Oxidation. *Chem. Soc. Rev.* **2013**, *42*, 2321−2337.
(14) Polo, A.; Lhermitte, C. R.; Dozzi, M. V.; Selli, E.; Sivula, K. Hydrogenation of $ZnFe_2O_4$ Flat Films: Effects of the Pre-Annealing Temperature on the Photoanodes Efficiency for Water Oxidation. *Surfaces* **2020**, *3*, 93−104.
(15) Lee, D. K.; Lee, D.; Lumley, M. A.; Choi, K. S. Progress on Ternary Oxide-Based Photoanodes for Use in Photoelectrochemical Cells for Solar Water Splitting. *Chem. Soc. Rev.* **2019**, *48*, 2126−2157.
(16) Lin, C.; Dong, C.; Kim, S.; Lu, Y.; Wang, Y.; Yu, Z.; Gu, Y.; Gu, Z.; Lee, D. K.; Zhang, K.; Park, J. H. Photo-Electrochemical Glycerol Conversion over a Mie Scattering Effect Enhanced Porous $BiVO_4$ Photoanode. *Adv. Mater.* **2023**, *35*, No. 2209955, DOI: 10.1002/adma.202209955.
(17) Pihosh, Y.; Turkevych, I.; Mawatari, K.; Uemura, J.; Kazoe, Y.; Kosar, S.; Makita, K.; Sugaya, T.; Matsui, T.; Fujita, D.; Tosa, M.; Kondo, M.; Kitamori, T. Photocatalytic Generation of Hydrogen by Core-Shell $WO_3/BiVO_4$ Nanorods with Ultimate Water Splitting Efficiency. *Sci. Rep.* **2015**, *5*, No. 11141.
(18) Kim, J. H.; Jang, J. W.; Jo, Y. H.; Abdi, F. F.; Lee, Y. H.; Van De Krol, R.; Lee, J. S. Hetero-Type Dual Photoanodes for Unbiased Solar Water Splitting with Extended Light Harvesting. *Nat. Commun.* **2016**, *7*, No. 13380.
(19) Gaillard, N.; Chang, Y.; Deangelis, A.; Higgins, S.; Braun, A. A Nanocomposite Photoelectrode Made of 2.2 EV Band Gap Copper Tungstate ($CuWO_4$) and Multi-Wall Carbon Nanotubes for Solar-Assisted Water Splitting. *Int. J. Hydrogen Energy* **2013**, *38*, 3166−3176.
(20) Polo, A.; Nomellini, C.; Grigioni, I.; Dozzi, M. V.; Selli, E. Effective Visible Light Exploitation by Copper Molybdo-Tungstate Photoanodes. *ACS Appl. Energy Mater.* **2020**, *3*, 6956−6964.
(21) Hill, J. C.; Ping, Y.; Galli, G. A.; Choi, K. S. Synthesis, Photoelectrochemical Properties, and First Principles Study of n-Type $CuW_{1-X}Mo_xO_4$ Electrodes Showing Enhanced Visible Light Absorption. *Energy Environ. Sci.* **2013**, *6*, 2440−2446.
(22) Yang, J.; Li, C.; Diao, P. Molybdenum Doped $CuWO_4$ Nanoflake Array Films as an Efficient Photoanode for Solar Water Splitting. *Electrochim. Acta* **2019**, *308*, 195−205.
(23) Lhermitte, C. R.; Bartlett, B. M. Advancing the Chemistry of $CuWO_4$ for Photoelectrochemical Water Oxidation. *Acc. Chem. Res.* **2016**, *49*, 1121−1129.
(24) Uemura, Y.; Ismail, A. S. M.; Park, S. H.; Kwon, S.; Kim, M.; Niwa, Y.; Wadati, H.; Elnaggar, H.; Frati, F.; Haarman, T.; Höppel, N.; Huse, N.; Hirata, Y.; Zhang, Y.; Yamagami, K.; Yamamoto, S.; Matsuda, I.; Katayama, T.; Togashi, T.; Owada, S.; Yabashi, M.; Halisdemir, U.; Koster, G.; Yokoyama, T.; Weckhuysen, B. M.; De Groot, F. M. F. Femtosecond Charge Density Modulations in Photoexcited $CuWO_4$. *J. Phys. Chem. C* **2021**, *125*, 7329−7336.
(25) Yourey, J. E.; Bartlett, B. M. Electrochemical Deposition and Photoelectrochemistry of $CuWO_4$, a Promising Photoanode for Water Oxidation. *J. Mater. Chem.* **2011**, *21*, 7651−7660.
(26) Grigioni, I.; Abdellah, M.; Corti, A.; Dozzi, M. V.; Hammarström, L.; Selli, E. Photoinduced Charge-Transfer Dynamics in $WO_3/BiVO_4$ Photoanodes Probed through Midinfrared Transient Absorption Spectroscopy. *J. Am. Chem. Soc.* **2018**, *140*, 14042−14045.
(27) Selim, S.; Francàs, L.; García-Tecedor, M.; Corby, S.; Blackman, C.; Gimenez, S.; Durrant, J. R.; Kafizas, A. $WO_3/BiVO_4$: Impact of Charge Separation at the Timescale of Water Oxidation. *Chem. Sci.* **2019**, *10*, 2643−2652.
(28) Pilli, S. K.; Deutsch, T. G.; Furtak, T. E.; Brown, L. D.; Turner, J. A.; Herring, A. M. $BiVO_4/CuWO_4$ Heterojunction Photoanodes for Efficient Solar Driven Water Oxidation. *Phys. Chem. Chem. Phys.* **2013**, *15*, 3273−3278.
(29) Ye, W.; Chen, F.; Zhao, F.; Han, N.; Li, Y. $CuWO_4$ Nanoflake Array-Based Single-Junction and Heterojunction Photoanodes for Photoelectrochemical Water Oxidation. *ACS Appl. Mater. Interfaces* **2016**, *8*, 9211−9217.
(30) Grigioni, I.; Corti, A.; Dozzi, M. V.; Selli, E. Photoactivity and Stability of $WO_3/BiVO_4$ Photoanodes: Effects of the Contact Electrolyte and of Ni/Fe Oxyhydroxide Protection. *J. Phys. Chem. C* **2018**, *122*, 13969−13978.
(31) Selim, S.; Francàs, L.; García-Tecedor, M.; Corby, S.; Blackman, C.; Gimenez, S.; Durrant, J. R.; Kafizas, A. $WO_3/BiVO_4$: Impact of Charge Separation at the Timescale of Water Oxidation. *Chem. Sci.* **2019**, *10*, 2643−2652.
(32) Grigioni, I.; Dozzi, M. V.; Selli, E. Photoinduced Electron Transfer in $WO_3/BiVO_4$ Heterojunction Photoanodes: Effects of the WO_3 Layer Thickness. *J. Phys.: Condens. Matter* **2020**, *32*, No. 014001.
(33) Grigioni, I.; Polo, A.; Dozzi, M. V.; Ganzer, L.; Bozzini, B.; Cerullo, G.; Selli, E. Ultrafast Charge Carrier Dynamics in $CuWO_4$ Photoanodes. *J. Phys. Chem. C* **2021**, *125*, 5692−5699.
(34) Cai, L.; Zhao, J.; Li, H.; Park, J.; Cho, I. S.; Han, H. S.; Zheng, X. One-Step Hydrothermal Deposition of Ni:FeOOH onto Photoanodes for Enhanced Water Oxidation. *ACS Energy Lett.* **2016**, *1*, 624−632.
(35) Thang, H. V.; Albanese, E.; Pacchioni, G. Electronic Structure of $CuWO_4$: Dielectric-Dependent, Self-Consistent Hybrid Functional Study of a Mott-Hubbard Type Insulator. *J. Phys.: Condens. Matter* **2019**, *31*, No. 145503, DOI: 10.1088/1361-648X/aaff3e.
(36) Sorenson, S.; Driscoll, E.; Haghighat, S.; Dawlaty, J. M. Ultrafast Carrier Dynamics in Hematite Films: The Role of Photoexcited Electrons in the Transient Optical Response. *J. Phys. Chem. C* **2014**, *118*, 23621−23626.
(37) Dey, S.; Ricciardo, R. A.; Cuthbert, H. L.; Woodward, P. M. Metal-to-Metal Charge Transfer in AWO_4 (A = Mg, Mn, Co, Ni, Cu, or Zn) Compounds with the Wolframite Structure. *Inorg. Chem.* **2014**, *53*, 4394−4399.
(38) Grigioni, I.; Polo, A.; Dozzi, M. V.; Stamplecoskie, K. G.; Jara, D. H.; Kamat, P. V.; Selli, E. Enhanced Charge Carrier Separation in $WO_3/BiVO_4$ Photoanodes Achieved via Light Absorption in the $BiVO_4$ Layer. *ACS Appl. Energy Mater.* **2022**, *5*, 13142−13148.
(39) Liang, Y.; Tsubota, T.; Mooij, L. P. A.; Van De Krol, R. Highly Improved Quantum Efficiencies for Thin Film $BiVO_4$ Photoanodes. *J. Phys. Chem. C* **2011**, *115*, 17594−17598.

Downloaded from pubs.acs.org/aaemcq/article-pdf/6/19/10020/2967344/ae3c01608.pdf by guest on 30 August 2026

(40) Abdi, F. F.; Van De Krol, R. Nature and Light Dependence of Bulk Recombination in Co-Pi-Catalyzed $BiVO_4$ Photoanodes. *J. Phys. Chem. C* **2012**, *116*, 9398−9404.
(41) Gao, Y.; Hamann, T. W. Quantitative Hole Collection for Photoelectrochemical Water Oxidation with $CuWO_4$. *Chem. Commun.* **2017**, *53*, 1285−1288.
(42) Shadabipour, P.; Raithel, A. L.; Hamann, T. W. Charge-Carrier Dynamics at the $CuWO_4$/Electrocatalyst Interface for Photoelectrochemical Water Oxidation. *ACS Appl. Mater. Interfaces* **2020**, *12*, 50592−50599.
(43) Chen, L.; Li, W.; Qiu, W.; He, G.; Wang, K.; Liu, Y.; Wu, Q.; Li, J. Oriented $CuWO_4$ Films for Improved Photoelectrochemical Water Splitting. *ACS Appl. Mater. Interfaces* **2022**, *14*, 47737−47746.
(44) Hu, D.; Diao, P.; Xu, D.; Xia, M.; Gu, Y.; Wu, Q.; Li, C.; Yang, S. Copper(II) Tungstate Nanoflake Array Films: Sacrificial Template Synthesis, Hydrogen Treatment, and Their Application as Photoanodes in Solar Water Splitting. *Nanoscale* **2016**, *8*, 5892−5901.
(45) Li, C.; Guo, B.; Peng, B.; Yue, C.; Diao, P. Copper Tungstate ($CuWO_4$) Nanoflakes Coupled with Cobalt Phosphate (Co-Pi) for Effective Photoelectrochemical Water Splitting. *Int. J. Electrochem. Sci.* **2019**, *14*, 9017−9029.
(46) Liu, Z.; Song, Q.; Zhou, M.; Guo, Z.; Kang, J.; Yan, H. Synergistic Enhancement of Charge Management and Surface Reaction Kinetics by Spatially Separated Cocatalysts and p-n Heterojunctions in Pt/$CuWO_4$/Co_3O_4 Photoanode. *Chem. Eng. J.* **2019**, *374*, 554−563.
(47) Li, C.; Diao, P. Boosting the Activity and Stability of Copper Tungsten Nanoflakes toward Solar Water Oxidation by Iridium-Cobalt Phosphates Modification. *Catalysts* **2020**, *10*, No. 913, DOI: 10.3390/catal10080913.
(48) Tian, C. M.; Jiang, M.; Tang, D.; Qiao, L.; Xiao, H. Y.; Oropeza, F. E.; Hofmann, J. P.; Hensen, E. J. M.; Tadich, A.; Li, W.; Qi, D. C.; Zhang, K. H. L. Elucidating the Electronic Structure of $CuWO_4$ Thin Films for Enhanced Photoelectrochemical Water Splitting. *J. Mater. Chem. A* **2019**, *7*, 11895−11907.
(49) Sun, Y.; Du, F.; Xie, D.; Yang, D.; Jiao, Y.; Jia, L.; Fan, H. Improved Water Oxidation via Fe Doping of $CuWO_4$ Photoanodes: Influence of the Fe Source and Concentration. *Chin. Phys. B* **2020**, *29*, No. 127801, DOI: 10.1088/1674-1056/aba9cb/meta.
(50) Bohra, D.; Smith, W. A. Improved Charge Separation via Fe-Doping of Copper Tungstate Photoanodes. *Phys. Chem. Chem. Phys.* **2015**, *17*, 9857−9866.
(51) Zhang, H.; Yilmaz, P.; Ansari, J. O.; Khan, F. F.; Binions, R.; Krause, S.; Dunn, S. Incorporation of Ag Nanowires in $CuWO_4$ for Improved Visible Light-Induced Photoanode Performance. *J. Mater. Chem. A* **2015**, *3*, 9638−9644.
(52) Li, C.; Diao, P. Fluorine Doped Copper Tungsten Nanoflakes with Enhanced Charge Separation for Efficient Photoelectrochemical Water Oxidation. *Electrochim. Acta* **2020**, *352*, No. 136471.
(53) Nair, V.; Perkins, C. L.; Lin, Q.; Law, M. Textured Nanoporous Mo:$BiVO_4$ Photoanodes with High Charge Transport and Charge Transfer Quantum Efficiencies for Oxygen Evolution. *Energy Environ. Sci.* **2016**, *9*, 1412−1429.
(54) Seabold, J. A.; Choi, K. S. Efficient and Stable Photo-Oxidation of Water by a Bismuth Vanadate Photoanode Coupled with an Iron Oxyhydroxide Oxygen Evolution Catalyst. *J. Am. Chem. Soc.* **2012**, *134*, 2186−2192.
(55) Polo, A.; Grigioni, I.; Magni, M.; Facibeni, A.; Dozzi, M. V.; Selli, E. Unravelling the Bulk and Interfacial Charge Transfer Effects of Molybdenum Doping in $BiVO_4$ Photoanodes. *Appl. Surf. Sci.* **2021**, *556*, No. 149759.
(56) Grigioni, I.; Stamplecoskie, K. G.; Selli, E.; Kamat, P. V. Dynamics of Photogenerated Charge Carriers in WO_3/$BiVO_4$ Heterojunction Photoanodes. *J. Phys. Chem. C* **2015**, *119*, 20792−20800.
(57) Zhao, J.; Cai, L.; Li, H.; Shi, X.; Zheng, X. Stabilizing Silicon Photocathodes by Solution-Deposited Ni-Fe Layered Double Hydroxide for Efficient Hydrogen Evolution in Alkaline Media. *ACS Energy Lett.* **2017**, *2*, 1939−1946.
(58) Higashi, T.; Nishiyama, H.; Suzuki, Y.; Sasaki, Y.; Hisatomi, T.; Katayama, M.; Minegishi, T.; Seki, K.; Yamada, T.; Domen, K. Transparent Ta_3N_5 Photoanodes for Efficient Oxygen Evolution toward the Development of Tandem Cells. *Angew. Chem., Int. Ed.* **2019**, *58* (8), 2300−2304.
(59) Su, J.; Feng, X.; Sloppy, J. D.; Guo, L.; Grimes, C. A. Vertically Aligned WO_3 Nanowire Arrays Grown Directly on Transparent Conducting Oxide Coated Glass: Synthesis and Photoelectrochemical Properties. *Nano Lett.* **2011**, *11*, 203−208.
(60) Polo, A.; Dozzi, M. V.; Grigioni, I.; Lhermitte, C.; Plainpan, N.; Moretti, L.; Cerullo, G.; Sivula, K.; Selli, E. Multiple Effects Induced by Mo^{6+} Doping in $BiVO_4$ Photoanodes. *Sol. RRL* **2022**, No. 2200349, DOI: 10.1002/solr.202200349.
(61) Ding, K.; Chen, B.; Fang, Z.; Zhang, Y.; Chen, Z. Why the Photocatalytic Activity of Mo-Doped $BiVO_4$ Is Enhanced: A Comprehensive Density Functional Study. *Phys. Chem. Chem. Phys.* **2014**, *16*, 13465−13476.

Downloaded from pubs.acs.org/aaemcq/article-pdf/6/19/10020/2967344/ae3c01608.pdf by guest on 30 August 2026